UNIVERSITY OF LEEDS

This is a repository copy of *Prediction of Permeability of Realistic and Virtual Layered Nonwovens using Combined Application of X-ray µCT and Computer Simulation*.

Accepted Manuscript

Title: Prediction of Permeability of Realistic and Virtual Layered Nonwovens using Combined Application of X-ray μCT and Computer Simulation

Authors: Parham Soltani, Mohammad Zarrebini, Reyhaneh Laghaei, Ali Hassanpour

Please cite this article as: Soltani, Parham, Zarrebini, Mohammad, Laghaei, Reyhaneh, Hassanpour, Ali, Prediction of Permeability of Realistic and Virtual Layered Nonwovens using Combined Application of X-ray μCT and Computer Simulation.Chemical Engineering Research and Design http://dx.doi.org/10.1016/j.cherd.2017.06.035

This is a PDF file of an unedited manuscript that has been accepted for publication. As a service to our customers we are providing this early version of the manuscript. The manuscript will undergo copyediting, typesetting, and review of the resulting proof before it is published in its final form. Please note that during the production process errors may be discovered which could affect the content, and all legal disclaimers that apply to the journal pertain.

Prediction of Permeability of Realistic and Virtual Layered Nonwovens using Combined Application of X-ray μCT and Computer Simulation

Parham Soltani[a*], Mohammad Zarrebini[a], Reyhaneh Laghaei[a], and Ali Hassanpour[b]

[a] Department of Textile Engineering, Isfahan University of Technology, Isfahan 83111 - 84156, Iran

[b] School of Chemical and Process Engineering, University of Leeds, LS2 9JT Leeds, UK

[*] Corresponding author. Tel.:+98 3133911093; fax: +98 3133912444.
E-mail address: Pa.soltani@cc.iut.ac.ir

Graphical abstract
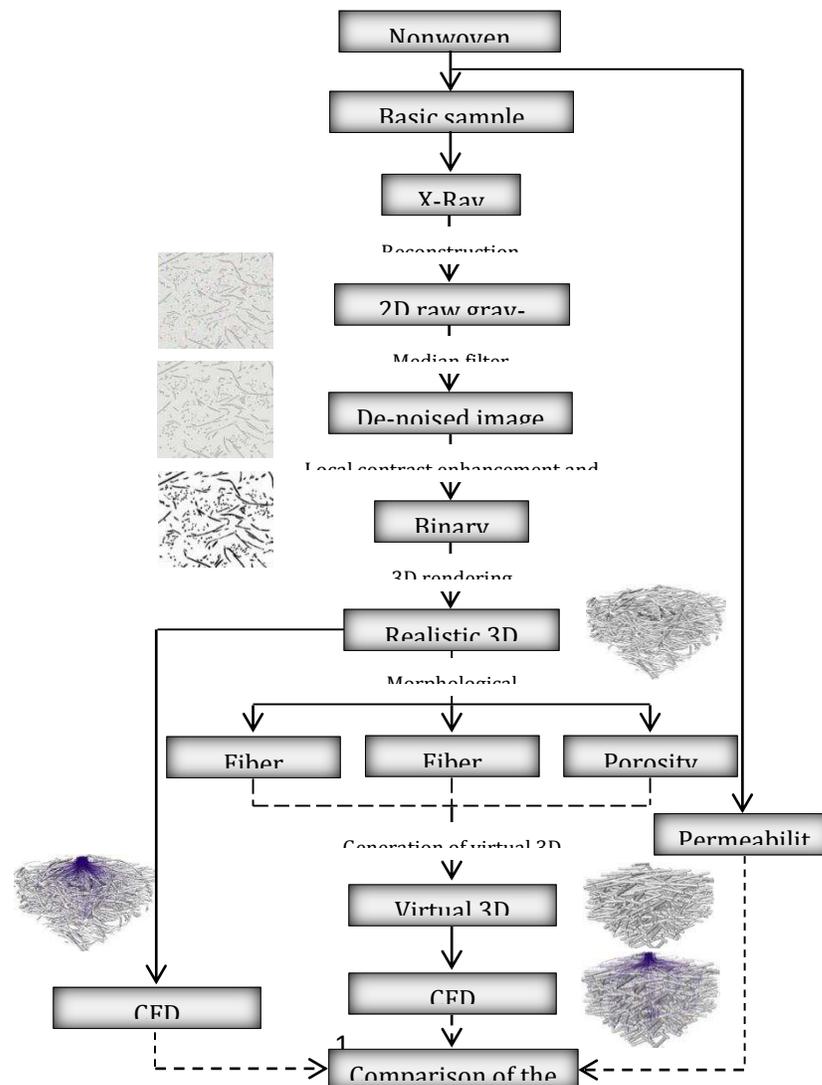
Highlights

- Combined application of X-ray μCT and computer simulation was introduced

- Algorithms were developed to extract morphological information of micro-structure

- A Matlab-based program capable of producing fibrous structures was developed

- Permeability of realistic and virtual layered nonwoven structures was determined

- Good agreement between the results and those of published literature was observed

Abstract

Fundamental understanding of transport properties of fibrous porous media is contingent upon in depth knowledge of their internal structure at the micro-scale. In this work computer simulations are explicitly coupled with X-ray micro-computed tomography (μCT) to investigate the effect of micro-structure on permeability of fibrous media. In order to reach this aim, samples of layered nonwoven fabrics were produced and realistic 3D images of their structure were prepared using X-ray μCT. A series of algorithms was developed to extract micro-structural parameters of fibrous media, including fibers population, orientation and diameter of each fiber as well as the local porosity of structure from high-resolution realistic 3D images. A Matlab-based program capable of producing fibrous structures with various fiber diameters, porosities, thicknesses and 3D fiber orientations was developed. The obtained parameters from μCT images were then implemented into the simulation code to generate virtual fibrous structures.

Prediction of permeability in realistic and virtual structures was done by fluid flow simulation through the micro-structure of porous media. The results indicated that both through- and in-plane permeabilities are strongly dependent on the porosity of structure. It was established that the anisotropic nature of the geometry creates anisotropic permeability, with a ratio of 1.8. The anisotropy effect was found to be more profound at higher porosity values. Comparison of numerical results with experimentally obtained data and those of empirical, analytical, numerical, and experimental models were made. Considering the porosity of structures, acceptable agreement between the results and previously published findings was observed.

Keywords: Micro-scale modeling; permeability; X-ray micro-computed tomography; realistic structure; virtual structure; porosity

Nomenclature

Δp:	Pressure drop across porous medium, Pa
Δt:	Thickness of porous medium, m
μ:	Dynamic viscosity, $Pa.s$
V:	Superficial velocity, m/s
K:	Permeability of porous medium, m^2
A	Cross-sectional area, m^2
ε:	Porosity, %
r:	Fiber radius, m
$\vec{P}$:	Unit vector
$\psi(\vec{P})$	probability density distribution function over orientation space
θ:	Angle between the fiber axis and z-axis, deg
φ:	Angle between the projection of the fiber on the $x - y$ plane and x-axis, deg
n:	Number of fibers
SVF:	Solid volume fractions, %
$\emptyset$:	Solid volume fractions, %
v_x:	Component of the velocity vector in x- direction
v_y:	Component of the velocity vector in y- direction
v_z:	Component of the velocity vector in z- direction
$\vec{V}$:	Velocity vector
p:	Pressure, Pa
θ_i:	Angle between the axis of ith fiber and z-axis, deg
φ_i:	Angle between the projection of the ith fiber on the $x - y$ plane and x-axis, deg
l_i:	Length of the ith fiber, $voxel$
l_{tot}:	Total fiber length, and the sum is over all fibers that comprise the RVE, $voxel$
RVE:	Representative volume element
Ω:	Orientation tensor
Ω_{xx}:	Quantity representing fiber alignment in the x-direction

Ω_{yy}:	Quantity representing fiber alignment in the y-direction
Ω_{zz}:	Quantity representing fiber alignment in the z-direction
$K_\perp$:	Through-plane permeability of porous medium, m^2
$K_\parallel$:	In-plane permeability of porous medium, m^2
K_1 and K_2:	Modified Bessel functions of second kind

1. Introduction

Nonwovens are fabrics manufactured directly from fibers by mechanical, chemical and thermal technologies. Structural complexity of these fabrics arises from the size and geometry of the fibers and particularly their spatial orientation which is largely dependent on the manufacturing method [1]. Nonwoven technologies are able to produce stable structures with very low solid volume fractions (SVFs). This unique feature of nonwovens is of considerable interest to a wide variety of applications in which fluid flow behavior is of great importance including, but not limited to, filtration industry [2-5], thermal insulation [6-8], acoustic insulation [9-11], fibrous composites [12-14], wipes [15-17], pulp and paper processing [18-20], and many other industrial and consumable products. In order to meet requirements for the above applications material designers should overcome engineering and development challenges during manufacturing steps to ensure product quality. Ability to predict the transport properties of nonwoven fabrics at the design stage is a valuable tool in the engineering of these materials [21].

If the *Reynolds* number is adequately small and laminar flow exists, the flow passing through porous media is governed by Darcy's law (Eq. (1)) [22]:

$$\frac{\Delta p}{\Delta t} = \frac{\mu V}{K} \tag{1}$$

where $\Delta p/\Delta t$ denotes the pressure gradient along the main flow direction, μ is the dynamic viscosity, V is the superficial velocity, and K is the permeability of porous medium.

Permeability is a measure of resistance offered by the micro-structure of porous medium to the fluid flow. It is intrinsic to the porous medium and is independent of the fluid type. For a fibrous medium, permeability depends on the porosity (ε), fiber radius (r), and orientation of the fibers relative to the flow direction [23].

Permeability of fibrous porous media has been investigated experimentally, analytically and numerically. An extensive review of these methods can be found in [24-26]. Early studies on flow through fibrous porous media were conducted experimentally and a

number of well-known models describing the permeability of porous media are based upon these experimentally obtained data. These studies generally describe permeability as a function of porosity and fiber radius, while ignoring the effect of fiber orientation distribution. Obviously two porous media of equal porosity, may have dramatically different permeabilities depending on their fiber orientation distribution [26]. Additionally, investigating the effect of pore-scale parameters on bulk properties requires a large experimental dataset, which is time-consuming and expensive to generate.

The analytical models generally idealize the fibrous porous medium as a matrix of cylindrical objects which are arranged in space in a defined periodic order. Under such assumption, a unit cell is identified and its permeability is determined by solution of established equations such as *Navier-Stokes*, usually in the limits of low and high porosity values [27]. Not only these idealized arrangements are far from complexity of real fibrous structures, but also the effect of inherent inhomogeneity of porosity and fiber orientation distribution in these idealized models are ignored. These models are mostly limited to the investigation of the creeping flow over a single cylinder with a limited boundary layer or through periodic fiber arrays [28, 29].

In the recent decade, modeling of fluid flow based on numerical simulation techniques using 3D geometries of fibrous structures has gained much attention. These techniques form accurate and powerful tools for solving established equations such as *Navier-Stokes* for 3D complex geometrical systems, particularly for fibrous porous media. Some authors have used virtual geometries to study fluid behavior [30-34]. These 3D geometries are usually constructed digitally using morphological information which is randomly extracted from statistical distributions, derived from 2D images of real structures. This process involves generation of virtual cylindrical objects whose diameters correspond to the diameter of fibers which are oriented at varying angles in a unit cell [35]. These techniques are valuable tools in investigation of the effect of micro-structure on fluid flow behavior. Since the morphological information is extracted from 2D images, the generated structures are still far from reality of fibrous structure. Additionally, numerical simulation studies that compare these models with their real counterparts scarcely exist.

Development of reliable fluid flow models have become possible during the last few years by introduction of computer-assisted, nondestructive imaging techniques such as X-ray micro-computed tomography (μCT) [36]. μCT is a reliable technique that three-dimensionally characterizes material micro-structure at micron level spatial resolution. The use of real geometries yields higher level of confidence as well as elimination of

unavoidable guesswork that is prerequisite for generation of virtual geometries. The advantage of combining μCT with numerical methods arises in the cases where direct experimental measurements are not feasible [37]. Studies on the effect of micro-structure on fluid flow within the real structure of nonwoven fibrous media are rather scarce and limited to the effect of porosity. This is attributed to the structural complexity of these materials [1, 38].

The dynamic of fluid flow and transport process is directly associated with micro-structure of fibrous medium. The structure at this scale is usually extremely irregular and difficult to characterize. Therefore, quantitative morphological information of the micro-structure, such as fiber orientation distribution, fiber diameter and porosity, is imperative to understand and model the very complex fluid flow in fibrous materials. While most available data on permeability of fibrous media are based on macro-scale phenomena and are often empirically-based, challenges still remain for fundamental researches at a much smaller length scale. Motivated by this scientific need, this paper pioneers the combined application of μCT and simulation techniques for generation of virtual fibrous structures. The method is based on the use of parameters obtained from μCT images to simulate virtual fibrous structures. Computational Fluid Dynamics (CFD) is used to solve *Navier-Stokes* equations for calculation of through- and in-plane permeability of realistic and virtual structures. The results are then compared with experimentally obtained data and those of available published empirical, analytical, numerical and experimental models.

2. Materials and methods

2.1. Nonwoven production

This study investigates permeability of layered nonwoven fabrics which have gained expanding use in insulation and filtration industries where fiber orientation and porosity are of paramount importance. The ability to engineer micro-structure and overall in-plane fiber orientation of layered nonwovens during the manufacturing stage can enable designs of these fabrics for various applications in technical fields. In these structures fiber axes lie randomly in the fabric plane ($x - y$ plane) with slight orientation along fabric thickness (z-direction).

Nonwoven samples were prepared using 12 denier 75 mm long melt staple polypropylene fibers at Mahoot Co. (Iran, Isfahan) [39]. In order to idealize web isotropy, fibers were processed on a 2.5-meter-wide double swift carding machine

equipped with randomizing rollers. The randomizing rollers disrupt the preferential orientation of fibers and redistribute fibers into a randomized web in which fibers lie randomly in $x - y$ plane. Layered fibrous batt was produced by feeding the randomized webs to an industrial horizontal cross-lapper. This procedure results in random and uniform distribution of fibers in the resultant fibrous batt. The fibers were then mechanically entangled to produce a needled nonwoven fabric by reciprocating felting needles through a moving batt of fibers in a laboratory needle loom. As the batt moves through the needling zone, more fibers are progressively entangled into a consolidated fibrous network and a coherent porous structure is formed. The needled nonwoven fabric was eventually taken-up by a pair of take-up rollers. Fig. 1 illustrates the basic principle of a needle loom.

Needling was carried out at punch densities of 10 and 20/cm² with needle penetration depth of 10 mm using Groz-Beckert felting needles 15×18×32×3 C333 G3007. In order to change porosity of the samples, the 3D layered fibrous samples were subjected to the action of a laboratory thermal calendaring machine. The calendaring operation was carried out at temperature of 140° and pre-set pressures of 1.5, 2.5, 3.5 and 4.5 bar.

2.2. Permeability test

Permeability tests were conducted according to British Standard BS 5636 using Shirley UK air permeability tester. The measurement principle consisted of applying a pressure drop (Δp) on a given cross-sectional area (A) of the sample. Once the flow reached the steady-state condition across the sample thickness (Δt), the air superficial velocity (V) was given by the apparatus. Permeability was then calculated using Darcy's law (Eq. (1)). Prior to the test, samples were conditioned at temperature of 20 ± 2°C and relative humidity of 65 ± 2% for 24 h. Laminar flow was achieved by applying a constant small pressure difference between the two sides of samples at 20 cm^2 test area. Under these conditions, the fluid is *Newtonian* with small *Reynolds* number of about 0.5 in which viscous forces dominate the inertial forces and hence Darcy's law is valid.

2.3. Image acquisition

X-ray micro-computed tomography (μCT) has its roots in Computerized Axial Tomography (CAT or CT) scan that has been widely used in medical applications for more than 50 years [40]. Rather than synchronous rotation of the X-ray source and detectors around the specimen, as in medical CT technology, in μCT imaging the

7

specimen is placed on a rotary holder. Additionally, instead of generating a series of two-dimensional sliced images from one-dimensional projections, a reconstructed three-dimensional image array is created directly from two-dimensional projections. The principle is based on image contrast which is produced by variations in the X-ray attenuation. When an X-ray beam passes through a sample, depending on the local density and compositional differences within the sample it is attenuated. A series of detectors accumulate all the energy of the transmitted photons and provide the numerical data required for reconstruction of an image [41-43]. Fig. 2 depicts the schematic illustration of μCT scanning device. Detailed descriptions of μCT technique is provided by researchers such as Lewitt [44] and Salvo et al. [45].

Image data for the nonwoven samples was acquired using the Phoenix Nanotom X-ray tomography system, housed in the School of Chemical and Process Engineering at University of Leeds. The device has been extensively used for the pore structure analysis and prediction of permeability of porous media [46-48]. Experimental samples were selected well away from the inherently non-uniform edges of fabric. Precautions were taken not to disturb the initial micro-structure of the samples before and during the test. Samples were fixed on a rotational holder which is located between the X-ray source and the detectors and progressively rotates over a total angular range (360°). Samples were illuminated in various directions. For each direction the projection of the attenuation coefficients was measured. Statistical errors were minimized by selecting and scanning of 5 samples from different locations across each nonwoven fabric. Collected raw data were then reconstructed with an ultra-high resolution noise-reducing filter back-projection algorithm. The scanning settings are given in Table 1.

2.4. Image pre-processing

In order to generate a stack of 2D cross-sectional images in gray-scale format, the 2D X-ray shadow images generated using X-ray tomography were compiled using CT-Analyzer software. The gray-scale images were then post-processed for noise reduction and transformation to binary images (segmentation) which are precursors for initiation of any calculation. The image post-processing algorithms were applied to gray-scale images using MATLAB R2011a Image Processing Toolbox (The Mathworks, Natick, MA). Gray-scale images from μCT comprise a certain level of noise. The noise reduction has a colossal effect on the quality of the subsequent segmentation process. The image processing initially was accomplished by reduction of image noise intensity using 3D median filter. The median filter technique applied with window size masking (3×3×3 in 3D) to smooth the volume voxel dataset.

In order to extract the fibre phase from the gray-scale images, a thresholding process must be performed. This in return results in a stack of binary images in which each voxel is assigned to either the fiber matrix or the void in the fibrous medium. The thresholding accuracy was improved by employing a local contrast enhancement procedure through histogram equalization prior to thresholding [21]. As the last step of image processing, a sequence of erosion and dilatation filters were applied to eliminate suspended particles. The full description of used image filters and tools can be found in [49]. Visualization of the reconstructed geometry is shown in Fig. 3.

2.5. Morphological analysis

Comprehensive understanding and complete analysis of architecture and topology of 3D fibrous structures obtained from μCT is an extremely challenging task. This is due to the enormous complexity and randomness of the structure. This section provides a series of techniques that can be used for morphological analysis of these structures.

2.5.1. *Porosity*

Once the 3D rendered volume was generated (Fig. 3), the first relevant micro-structure descriptor, i.e. the porosity, can simply be estimated by the ratio of number of voxels of the void phase to the total number of voxels in the structure.

2.5.2. *Skeletonization*

In order to extract fiber orientation distribution from a 3D fibrous structure, the reconstructed fiber surfaces must first be simplified to their medial axes or 'skeletons'. The medial axis offers a skeletal representation of the surface, while preserving the inherent geometric skeletal shape of the structure [50]. The skeletonization algorithm used in this work is similar to the one detailed by Viguié et al. [51]. Briefly, the 3D distance map of the thresholded image was calculated. The watershed technique was used to separate the fibers in the binary image. This algorithm simulates the flooding from a set of labeled regions in a 2D or 3D image. The regions are expanded according to a priority map and the objects are separated by a simple threshold on this map. Upon separation step, medial axes of fibers were computed using an efficient 3D thinning algorithm. The algorithm is ordered according to the distance map input and reduces the

dimensionality of 3D image by iterative removing of voxels from the volume provided that:

1- Voxel is a surface voxel;
2- Voxel is not end of line;
3- removing a voxel does not create hole in the object or change the number of connected component.

The algorithm output is a set of medial axes which is topologically equivalent to the original image and is one voxel wide. When two fibers bond at an acute angle of incidence, the resultant medial axes can be ladder-shaped and contain considerable number of spurious paths. The elimination of these paths was carried out using the "surface remnant reduction algorithm" of Yang and Lindquist as indicated in Fig. 4 [52].

Noise on centerlines was reduced by applying an average weighted filter. These treatments result in skeleton of the structure (Fig. 5), which is prerequisite for quantitative analysis of fiber orientation and diameter distribution. Details of the skeletonization algorithm used in this work are explained in [53, 54].

2.5.3. *Three-dimensional fiber orientation*

Physical, mechanical and transitional properties of fibrous porous media depend on the inherent properties and orientation of the constituent fibers. Despite availability of enormous research works on 2D analysis of fiber orientation in nonwoven fabrics [55-59], there are a few investigations on 3D fiber orientation of these materials. In this work, the "2D skeleton-based direct tracking algorithm" proposed by Pourdeyhimi et al. [55] and Komori and Marishima [60] was modified and adopted for 3D determination of fiber orientation [52]. In this algorithm, fibers are divided into small segments of length λ. This length is sufficiently shorter than the minimum wave of fiber crimp. These small segments may be replaced with the best-fitting straight line hereafter called straight fiber segment. Thus crimp path of fibers is presumed to consist of these straight segments. It is essential to define the minimum acceptable length of straight fiber segments. Segments smaller than the defined minimum length, ought to be discarded as noise. Upon transformation of the fibers crimp from non-linear to linear, fiber orientation can be measured. This is achieved by determination of individual straight fiber segments orientation. The unique spatial orientation of each fiber segment was defined by a unit vector $\vec{P}$ which lies on each segment as follow:

$$\vec{P} = \begin{pmatrix} \sin\theta\cos\varphi \\ \sin\theta\sin\varphi \\ \cos\theta \end{pmatrix} \tag{2}$$

where $0 \le \theta \le \pi$ is the angle between the fiber segment and the z-axis, and $0 \le \varphi \le 2\pi$ is the angle between the projection of the fiber segment on the $x - y$ plane and the x-axis.

The orientation state of a group of n fibers can be represented by the second-order tensor, Ω_{ij}, which is calculated by forming dyadic products of the vector $\vec{P}$ and then integrating the product of the resulting tensors with the probability distribution function over all possible directions of $\vec{P}$. The orientation tensor is calculated as follow:

$$\Omega_{ij} = \int_P P_i P_j \psi(\vec{P})d\vec{P} \tag{3}$$

where $\psi(\vec{P})$ is the probability density distribution function over orientation space, defined as the probability of a fiber lying within a range P and $P + dP$ [61].

Second-order fiber orientation tensor (Ω) was adopted to describe the 3D orientation of structures:

$$\Omega = \frac{1}{l_{tot}} \sum l_i \begin{bmatrix} \sin^2\theta_i\cos^2\varphi_i & \sin^2\theta_i\sin\varphi_i\cos\varphi_i & \cos\theta_i\sin\theta_i\cos\varphi_i \\ \sin^2\theta_i\sin\varphi_i\cos\varphi_i & \sin^2\theta_i\sin^2\varphi_i & \cos\theta_i\sin\theta_i\cos\varphi \\ \cos\theta_i\sin\theta_i\cos\varphi_i & \cos\theta_i\sin\theta_i\cos\varphi_i & \cos^2\theta_i \end{bmatrix} \tag{4}$$

where $0 \le \theta_i \le \pi$ is the angle between the axis of ith fiber segment and the z-axis, $0 \le \varphi_i \le 2\pi$ is the angle between the projection of the ith fiber segment on the $x - y$ plane and the x-axis, l_i denotes the length of the ith fiber segment, l_{tot} is the total fiber length, and the sum is over all fibers that comprise the representative volume element (RVE).

The values of each of diagonal elements of the tensor stand for the relative orientation in one of the co-ordinate axis i.e. x-, y- and z-directions. The trace of Ω is always unity. Therefore, for isotropic structures $\Omega_{xx} = \Omega_{yy} = \Omega_{zz} = 0.33$, and for idealistic layered structures $\Omega_{xx} = \Omega_{yy} = 0.5$ and $\Omega_{zz} = 0$

In order to evaluate the accuracy of developed algorithms, 3D fibrous structures with known spatial orientation were simulated and the developed algorithms were applied to them. Detailed information about fiber orientation determination algorithm can be found in [52].

2.5.4. *Fiber diameter*

Fiber diameter was determined using the medial axes and distance map of the input binary images. In a distance map the value of each voxel is equal to the distance to the nearest border voxel. The medial axis calculated by skeletonization algorithm was overlaid on top of the distance transformed image and fiber diameter was determined. Detailed explanation about skeleton-based fiber diameter determination algorithm can be found in [62].

2.6. Generation of virtual 3D fibrous structures

Virtual 3D fibrous structures were generated using a purposely developed Matlab-based program. Virtual 3D structures were simulated with a predefined SVF value, namely $\emptyset$ corresponding to the SVF of the realistic structures. Input parameters for the generated structures were SVF, 3D fiber orientation distribution and fiber diameter distribution. In accordance to the work of Nabovati et al. [28] and Wang et al. [30] the negligible effect of fibre curvature on the permeability of the medium was ignored. Therefore, inside the micro-structure, fibers were simulated like an infinite length cylinder. Each fiber was defined by its diameter and spatial orientation. These parameters were extracted from statistical information derived from the morphological analysis of realistic 3D images. Generated fibers were placed in a simulation box with defined dimensions. The SVF of generated structure was varied by adding or subtracting fibers to or from the simulation box. At first, the SVF of simulation box is 0. Fibers with defined orientation are added sequentially to the simulation box until the SVF of the generated structure reaches the desired value of $\emptyset \pm 0.005$. If the added fiber causes the value of SVF to exceed $\emptyset + 0.005$, the added fiber is removed and another fiber is added. The procedure continues until the desired SVF is reached.

Generated fibers were allowed to interpenetrate when were placed in the simulation box. Analysis of realistic μCT images demonstrated that the fibrous media were of sufficiently low density and therefore the amount of overlaps can be ignored. This amount can be easily quantified by calculating the difference between the volume of the generated fibers and that of fibers placed in the simulation box. The entire fibrous structure was discretized by a uniform Cartesian grid with edge length of 3 μm (voxel size is 3 μm). Fig. 6 depicts an example of generated virtual layered fibrous structure.

2.7. Fluid flow simulation in virtual and realistic structures

Fluid flow was simulated by numerically solving incompressible creeping *Newtonian* flow through the 3D pore space of realistic and virtual structures. Fluid flow domains were meshed using voxel-based approach which directly generates a volumetric mesh based on the voxelised scan data. Detailed description of voxel-based methodology is given in authors' previous studies [63, 64].

To reflect the representativeness of the computational domains, the Brinkman screening length, which is given by the square root of the permeability ($\sqrt{K}$), was used as a qualitative criterion. In order to smooth out the local heterogeneities, in accordance with the work of Clague and Phillips [65], a simulation domain size with 14 times greater than the Brinkman's screening length is needed. In this work, the simulation domain size was chosen such that the domain size was at least $20\sqrt{K}$ which is larger than that of RVE determined in other researches [1, 23, 66]. In order to ensure that the results are independent of the domain size, results based on domain sizes greater than $20\sqrt{K}$ were compared and no significant variation in the ensemble average permeability of the media was observed. Thus, it can be said that the results truly represent the permeability of the fibrous media at macro-scale. Permeability K can be estimated in advance with the widely accepted Davies's correlation equation which is often used by the community of air filtration [67]:

$$\frac{K}{r^2} = \left[16\sqrt{(1-\varepsilon)^3}(1 + 56(1-\varepsilon)^3)\right]^{-1} \tag{5}$$

where r and ε represent fiber radius and porosity of the medium, respectively.

Flow regime was regulated by maintaining a small constant pressure difference of 50 Pa between the inlet and outlet boundaries of the model system, causing *Navier-Stokes flow* to prevail. Under this condition the governing equations for conservation of mass and momentum are as follows:

$$\frac{\partial v_x}{\partial x} + \frac{\partial v_y}{\partial y} + \frac{\partial v_z}{\partial z} = 0 \tag{6}$$

$$\frac{\partial p}{\partial x} = \mu \left(\frac{\partial^2 v_x}{\partial x^2} + \frac{\partial^2 v_x}{\partial y^2} + \frac{\partial^2 v_x}{\partial z^2}\right) \tag{7}$$

$$\frac{\partial p}{\partial y} = \mu \left(\frac{\partial^2 v_y}{\partial x^2} + \frac{\partial^2 v_y}{\partial y^2} + \frac{\partial^2 v_y}{\partial z^2}\right) \tag{8}$$

13

$$\frac{\partial p}{\partial z} = \mu \left(\frac{\partial^2 v_z}{\partial x^2} + \frac{\partial^2 v_z}{\partial y^2} + \frac{\partial^2 v_z}{\partial z^2} \right) \tag{9}$$

where v_x, v_y and v_z represent the three components of the velocity vector $\vec{V}$ in the x-, y- and z-directions, p denotes pressure, and μ is viscosity of fluid. The calculations were performed using the viscosity of air (1.98×10^{-5} $Pa.s$) as required by the simulation.

Laboratory-like environment was simulated by imposing the following boundary conditions:

- no-slip state at fluid-solid interfaces within the medium;
- isolation of the medium from the surroundings. This was done by addition of one-voxel-wide plane of solid phase with no-slip condition on the image faces which are along the main flow direction
- standard fixed-pressure at the outlet
- standard fixed-pressure at the inlet

Once the flow reached a statistically stationary state, the superficial velocity through the domain, in the direction of the pressure gradient, was computed by solving *Navier-Stokes* equations. Using a desktop workstation with 64 GB of RAM and 16 processors, each simulation session was completed within the time span of 2 to 3 h.

Permeability was then calculated using Darcy's law. In order to compare the obtained results with those of experimental, analytical and numerical works, computed permeabilities were non-dimensionalized by the square of the fiber radius. The common mean absolute percentage error (MAPE) was used to assess the prediction performance of virtual model. Fig. 7 illustrates the flow chart of the work.

3. Results and discussions

Table 2 presents the structural characteristics of realistic structures and their virtual structures counterparts.

The non-zero values of Ω_{zz} in Table 2 point to the slight orientation of fibers in the z-direction, indicating that the investigated nonwoven samples are not idealistic layered structures. Additionally, the almost similar values of Ω_{xx} and Ω_{yy} point to the random orientation of fibers in the $x-y$ plane. The results also indicate that as far as the 3D fiber orientation and porosity of the structures are concerned, the realistic structures and their virtual counterparts are micro-structurally identical, provided that the effect of fiber curvature is ignored.

CFD simulations for realistic and virtual samples were performed for flow in the z-direction (through-plane) and x- and y-directions (in-plane). The results of CFD simulations together with the path lines of fluid flow through the structures are presented in Fig. 8. Flow streamlines in x-, y- and z-directions are shown in different colors. As can be observed, flow is both complex and highly three-dimensional. This is due to the complex and highly interconnected structure of the nonwoven fabrics.

Calculated permeabilities were non-dimensionalized via division by the square of fiber radius. This is required for comparison of the results with those of empirical, analytical, numerical and experimental works. Fig. 9 depicts through-plane dimensionless permeability of realistic and virtual structures versus porosity. Since dimensionless permeability is sensitive to the changes in porosity, log-scale ordinates were used. Standard deviations are omitted as are indiscernible in the scale of the plot.

As can be observed, the normalized permeability tends to decrease non-linearly with decrease in medium porosity. By decreasing porosity of medium (increasing SVF), fluid penetrates into more tortuous paths and hence permeability decreases. The results also indicate that for all porosity values, there exists a good agreement between calculated permeabilities of realistic and virtual structures (MAPE of 8.8%). It can also be stated that, generally through-plane dimensionless permeabilities of virtual models are higher than those of realistic models. This may be attributed to the fact that in virtual models the effect of fiber curvature is ignored. Curvature of fibers increases complexity of fibrous structure and consequently affects permeability. The effect of degree of fiber curvature is currently being investigated by the authors, the results of which are due to be reported. The results of both models are in line with the trends of experimental data over the investigated range of porosity. It must be noted that the size of the samples that can be used in Shirley permeability tester is much larger than those considered in our micro-scale models and hence comparison is valid over a narrow porosity range of 0.83 to 0.89.

In order to further elucidate the argument, the results were compared with those of available published empirical, analytical, numerical and experimental studies. The results are depicted in Fig. 10.

Davies [67] presented measurement of the resistance to transverse flow through layered fibrous materials comprise of glass wool, glass rods, cotton, wool, camel hair, kapok, merino wool, rayon, and mixture of glass wool and copper wire. He proposed an empirical correlation, (Eq. (5)), fitting through-plane permeability data for the flow in highly porous fibrous media ($e > 0.70$). As is observed, for porosity range of $0.77 < \varepsilon < 86$ the expression shows an excellent agreement with those of realistic model. However, at higher porosity values the through-plane permeability tends to be under-predicted.

Tomadakis and Robertson [68] used a conduction-based analytical method to investigate flow behavior in fibrous media. The following equation was proposed for prediction of through-plane permeability in layered structures for porosity values of $\varepsilon > 0.70$:

$$\frac{K_\perp}{r^2} = \frac{\varepsilon(\varepsilon - 0.11)^{2.785}}{8 \ln^2 \varepsilon \, (0.89)^{0.785}[(1.785)\varepsilon - 0.11]^2} \tag{10}$$

where $K_\perp$ and ε represent the through-plane permeability and porosity of medium, respectively and r is fiber radius.

The results indicate that for porosity values over 0.80 the simulated permeabilities are consistent with the predicted results obtained by Eq. (10).

Using swarm theory, Spielman and Goren [69] proposed the following analytical equation for the permeability of fibrous materials with fibers laid randomly in the plane perpendicular to the direction of superficial flow:

$$\frac{1}{(1 - \varepsilon)} = 2 + \frac{4\sqrt{K_\perp}}{r} \frac{K_1\left(\frac{r}{\sqrt{K_\perp}}\right)}{K_2\left(\frac{r}{\sqrt{K_\perp}}\right)} \tag{11}$$

where $K_\perp$ denotes through-plane permeability of the medium, K_1 and K_2 are the modified Bessel functions of second kind, and r and ε represent fiber radius and porosity of medium, respectively.

Tamayol and Bahrami [70] employed a scale analysis technique for determination of through-plane permeability of layered structures and proposed the following analytical equation:

$$\frac{K_\perp}{r^2} = 0.032\sqrt{\varepsilon}\left[\left(\frac{\pi}{4(1-\varepsilon)}\right)^2 - \frac{\pi}{2(1-\varepsilon)} + 1\right] \tag{12}$$

The results indicate that for all values of porosity, the equations of Spielman and Goren [69] and Tamayol and Bahrami [70] under-predict the permeability of layered structures. These analytical works are based on the perfectly layered structures in which fibers axes lie randomly in the plane perpendicular to the fluid flow ($x - y$ plane). However, as shown in Fig.3 and Table 2, realistic and virtual layered nonwoven fabrics cannot be considered to be ideal structures due to the slight orientation of fibers along fabric thickness. This contributes to the observed deviations between the CFD and analytical results, as demonstrated in Fig. 10.

Van Doormaal and Pharoah [34] used lattice Boltzmann method (LBM) to simulate the flow through an idealized proton exchange membrane fuel cell. Permeability of layered structures was determined by solving the flow at micro-structure level. The results yielded to the correlation in Eq. (13) for through-plane permeability of layered fibrous media for the porosity range of $0.60 < \varepsilon < 80$. The results are plotted in Fig. 10.

$$\frac{K_\perp}{r^2} = 0.028\,\frac{\varepsilon^{4.3}}{1-\varepsilon} \tag{13}$$

As can be observed, the results of CFD models are in good agreement with the correlation of Van Doormaal and Pharoah [34] for the porosity range of $0.60 < \varepsilon < 0.84$.

Comparison of the results were also made with CFD model of Zobel and his associates [32] conducted on virtual spun-bonded nonwoven fabrics. In order to simulate nonwoven fabrics, fibers were assumed to have a square cross-section and positioned horizontally in the x- or y-directions. These assumptions account for the large deviations between the results of CFD models and those of Zobel et al. [32].

Fluid flow behavior in hydroentangled nylon nonwoven fabrics was investigated by Jaganathan et al. [1]. An integrated approach using automated serial sectioning technique, digital volumetric imaging (DVI), together with CFD simulation was used. Realistic images of samples obtained via DVI technique and permeability of the samples was computed using CFD simulation. Agreement between our models and realistic model of Jaganathan et al. [1] is generally not satisfactory, particularly for $\varepsilon > 0.88$. DVI is a block-face fluorescence imaging technique where samples are embedded in a standard resin that has been modified to be opaque. After curing, in an automated process, embedded specimens are repeatedly sectioned using a diamond blade microtome and digitally imaged by epifluorescence microscope. The 2D cross-sections

are then combined to construct a 3D image of the micro-structure. In this study, hydroentangled fabrics were considered to be layered structures. The validity of this claim is not readily obvious since fibers in a hydroentangled fabric are bonded together in all x-, y-, and z-directions as a result of the impaction with the high-speed water jets. Additionally, due to the resin impregnation and sectioning operation samples are susceptible to micro-structural changes. All these could contribute to the deviation between the CFD models and realistic model of Jaganathan and his associates [1] as demonstrated in Fig. 10.

In order to enhance the aim of this research and provide a comprehensive treatment of the subject, the results were also compared with experimental data of:

- Jaganathan et al. [1] on nylon hydroentangled fabrics;
- Gostick and et al. [71] on carbon fiber electrode backing layers;
- Labrecque [72] on fibrous porous mats;
- Kostornov and Shevchuk [73, 74] on porous metal fiber materials;
- Young et al. [75] on glass fiber mats.

Apart from the work of Kostornov and Shevchuk [73, 74], acceptable agreement was found to exist between the CFD models and the results of above researchers.

Fig. 11 depicts in-plane dimensionless permeability of realistic and virtual structures versus porosity. Calculations were performed for flow in x- and y-directions. Comparison of permeabilities in the above two directions is not statistically significant, which is in line with random orientation of fibers in x–y plane as shown in Table 2.

It can be seen that in-plane permeability is highly dependent on porosity of medium. Results point to the existence of good agreement between the realistic and virtual models (MAPE of 6.9%). Since Shirley permeability tester is not capable of measuring in-plane permeability, thus simulation results were not compared with experimental data. Validity of the results was examined by comparing the simulation results with available analytical, numerical and experimental data in the literature. It appears that no other model for the in-plane permeability of layered structures of $0.65 < \varepsilon < 95$ is available that can be reduced to the form of K/r^2 apart from those shown in Fig. 11.

In-plane flow through layered structures for porosities higher than 0.70, can be calculated by the following analytical equation that was suggested by Tomadakis and Robertson [68]:

$$\frac{K_\parallel}{r^2} = \frac{\varepsilon(\varepsilon - 0.11)^{2.521}}{8\ln^2\varepsilon\,(0.89)^{0.521}[(1.521)\varepsilon - 0.11]^2} \tag{14}$$

where $K_\parallel$ represents in-plane permeability of the medium.

Comparison of the results points to the existence of reasonable agreement between the developed models and conduction-based model of Tomadakis and Robertson [68].

The results were also compared with analytical model of Tamayol and Bahrami [76]. This model assumes that the micro-structure of fibrous structure is a combination of equally-sized, equally-spaced fibers parallel to the flow. The in-plane permeability of such medium is estimated using a blending technique:

$$\frac{K_\parallel}{r^2} = 4\exp(\frac{46.6\,\varepsilon - 43.25}{-10.5\,\varepsilon^2 + 10.56\,\varepsilon + 1}) \tag{15}$$

As in the case of through-plane permeability, no acceptable agreement between the developed models and analytical model of Tamayol and Bahrami [76] is observed. This may be attributed to the very simple and idealistic structure assumed by them.

Van Doormaal and Pharoah [34] proposed the following correlation for the in-plane permeability of layered fibrous media for the porosity range of $0.60 < \varepsilon < 80$. In Fig. 11, the equation is plotted for the porosity range of $0.60 < \varepsilon < 0.95$.

$$\frac{K_\parallel}{r^2} = 0.026\,\frac{\varepsilon^{3.6}}{1 - \varepsilon} \tag{16}$$

As can be observed, for the porosity range of $0.73 < \varepsilon < 0.82$, the developed models correlate very well with the results of Van Doormaal and Pharoah [34].

The results were also compared with the finite element simulation results of Gauvin et al. [77] proposed for the in-plane permeability of layered strand mats. For porosity values less than 0.90 an excellent agreement between the results of the developed models and those of Gauvin et al. [77] is observed. It was argued that for higher porosity values these structures suffer from lack of homogeneity which results in variation of permeability.

Young and his associates [75] performed CFD numerical simulation of in-plane permeability of fibrous mats. Large deviations are observed between the developed models and simulation results of Young et al. This may be attributed to the strong velocity effect in their simulation.

Considering Fig. 11 where experimental data of Shih and Lee [78]; Feser et al. [79], and Gostick et al. [71] are shown, it can be stated that the developed realistic and virtual models successfully capture the trends of experimental data for the porosity range of $0.73 < \varepsilon < 0.87$. It is noteworthy that so far no universally agreed standard experimental setup exists for measuring the in-plane permeability of fibrous materials. This is the reason behind the diversities observed in the published experimental results.

The calculated in-plane and through-plane dimensionless permeabilities of realistic and virtual structures are plotted in Fig. 12. It was found that the layered structures exhibit anisotropic flow behavior with an anisotropy ratio ($K_{\parallel}/K_{\perp}$) of approximately1.8. This is consistent with the recent work of Tomadakis and Robertson [68]. This article claims that for layered structures the in-plane permeability is almost twice the through-plane permeability. As can be observed, the anisotropy effect is more pronounced for high porosity values. Structural changes imposed during calendaring operation are likely to affect anisotropy. Changes in anisotropy due to the compression are not yet fully understood, although data sets in this study point to the inverse relation between anisotropy and compression of the fibrous media.

The results point to the fact that anisotropic permeability is due to the anisotropic nature of geometry, suggesting that aligning the fibers in a certain direction leads to the change in the degree of anisotropy of structure. The inherent ability of nonwoven manufacturing process allows spatial orientation of fibers to be controlled and hence allows precise design of engineered fabrics for applications in which the fluid flow behavior is of importance.

Findings of the present work effectively can be used in optimization of liquid composite molding manufacturing processes, design and production of filter media, design and manufacture of adsorbent materials, pulp and paper processing, polymer industry and physiological systems and processes.

4. Conclusion

The study of fluid behavior in fibrous porous media is of considerable interest to a wide variety of industrial applications due to their high degree of flexibility and compressibility. Many experimental and analytical investigations have been conducted on permeability of fibrous structures. Experimental works despite their importance cannot capture the details of micro-scale flow-pattern in the porous media. Analytically developed models are not fully capable of apprehending the physical actuality of fibrous

structure. Most of these models are not general and fail to predict permeability over the wide range of porosities. With the aim of overcoming these limitations, numerical simulation methods have been proposed. These models are capable of predicting permeability of media by solving the fluid flow within the micro-structure of porous media. The development of these micro-scale models is contingent upon availability of quantitative morphological information of the micro-structure.

This work pioneers the combined application of μCT and simulation technique for generation of 3D virtual fibrous structures. 3D architecture of nonwoven structures was obtained using μCT. Micro-structural parameters including fibers population, orientation and diameter of each fiber as well as the porosity of medium were quantified. These parameters were then implemented into the developed simulation code and virtual 3D fibrous structures were generated.

Through- and in-plane permeabilities of realistic and virtual fibrous structures were calculated via simulation of fluid flow through the micro-structure of media using CFD tools. The results were compared with experimental data as well as those of available empirical, analytical, numerical and experimental works. Acceptable agreement was found to exist between the CFD results and published models. Additionally, the sources of discrepancy observed in the results were discussed. The results indicated that the porosity of medium strongly affects both through- and in-plane permeabilities. It was concluded that the anisotropy of the layered media creates anisotropic permeability. The in-plane permeability was found to be nearly 1.8 times greater than the through-plane permeability. The anisotropy effect was found to be more remarkable for higher porosity values.

References

[1] S. Jaganathan, H. Vahedi Tafreshi, B. Pourdeyhimi, A Realistic Approach for Modeling Permeability of Fibrous Media: 3-D Imaging Coupled with CFD Simulation, Chem. Eng. Sci., 63 (2008) 244-252.

[2] P.C. Gervais, N. Bardin-Monnier, D. Thomas, Permeability Modeling of Fibrous Media with Bimodal Fiber Size Distribution, Chem. Eng. Sci., 73 (2012) 239-248.

[3] S. Jaganathan, H. Vahedi Tafreshi, B. Pourdeyhimi, On the Pressure Drop Prediction of Filter Media Composed of Fibers with Bimodal Diameter Distributions, Powder Technol., 181 (2008) 89-95.

[4] A.K. Pradhan, D. Das, R. Chattopadhyay, S.N. Singh, Effect of 3D Fiber Orientation Distribution on Particle Capture Efficiency of Anisotropic Fiber Networks, Powder Technol., 249 (2013) 205-207.

[5] A. Charvet, Y. Gonthier, A. Bernis, E. Gonze, Filtration of Liquid Aerosols with a Horizontal Fibrous Filter, Chem. Eng. Res. Des., 86 (2008) 569-576.

[6] I. Budaiwi, A. Abdou, The Impact of Thermal Conductivity Change of Moist Fibrous Insulation on Energy Performance of Buildings Under Hot–humid Conditions, Energy Build., 60 (2013) 388-399.

[7] A. Abdou, I. Budaiwi, The Variation of Thermal Conductivity of Fibrous Insulation Materials Under Different Levels of Moisture Content, Constr. Build. Mater., 43 (2013) 533-544.

[8] S. Mahjoob, K. Vafai, A Synthesis of Fluid and Thermal Transport Models for Metal Foam Heat Exchangers, Int. J. Heat Mass Transfer, 51 (2008) 3701-3711.

[9] F. Shahani, P. Soltani, M. Zarrebini, The Analysis of Acoustic Characteristics and Sound Absorption Coefficient of Needle Punched Nonwoven Fabrics, J. Eng. Fibers Fabr., 9 (2014) 84-92.

[10] M. Tascan, E.A. Vaughn, Effects of Total Surface Area and Fabric Density on the Acoustical Behavior of Needlepunched Nonwoven Fabrics, Text. Res. J., 78 (2008) 289-296.

[11] B. Schnitta, Study to Optimize Speech Clarity in a Hospital Pediatric Trauma Room, using Newly Patented Tuning Tube and a Custom Nonwoven Fabric, J. Acoust. Soc. Am., 135 (2014) 2403-2403.

[12] R. Laghaei, M. Zarrebini, P. Soltani, Axial and Transverse Permeability of Unidirectional Fiber Reinforced Composites, J. Text. Inst., In Press (2017).

[13] S. Sharma, D.A. Siginer, Permeability Measurement Methods in Porous Media of Fiber Reinforced Composites, Appl. Mech. Rev., 63 (2010) 020802-020802.

[14] D. Xue, M. Miao, H. Hu, Permeability Anisotropy of Flax Nonwoven Mats in Vacuum-assisted Resin Transfer Molding, J. Text. Inst., 102 (2011) 612-620.

[15] C. Sun, D. Zhang, L.C. Wadsworth, M. McLean, Development of Innovative Cotton-surfaced Nonwoven Laminates, J. Ind. Text., 31 (2002) 179-188.

[16] R. Kumar, D. Moyo, R.D. Anandjiwala, Viscose Fabric Bonded with Soy Protein Isolate by Foam Application Method, J. Ind. Text., 44 (2015) 849-867.

[17] S. Nam, R. Slopek, D. Wolf, M. Warnock, B.D. Condon, P. Sawhney, E. Gbur, M. Reynolds, C. Allen, Comparison of Biodegradation of Low-weight Hydroentangled Raw Cotton Nonwoven Fabric and that of Commonly used Disposable Nonwoven Fabrics in Aerobic Captina Silt Loam Soil, Text. Res. J., (2015).

[18] C. Antoine, P. Nygård, Ø.W. Gregersen, R. Holmstad, T. Weitkamp, C. Rau, 3D images of Paper Obtained by Phase-contrast X-ray Microtomography: Image Quality and Binarisation, Nucl. Instrum. Methods Phys. Res., Sect. A, 490 (2002) 392-402.

[19] J. Ghassemzadeh, M. Sahimi, Pore Network Simulation of Fluid Imbibition into Paper during Coating: II. Characterization of Paper's Morphology and Computation of its Effective Permeability Tensor, Chem. Eng. Sci., 59 (2004) 2265–2280.

[20] J. Hyvaluoma, P. Raiskinmaki, A. Jasberg, A. Koponen, M. Kataga, J. Tomenon, Simulation of Liquid Penetration in Paper, Phys. Rev. E: Stat. Nonlinear Soft Matter Phys., 73 (2006) 036705-036712.

[21] P. Soltani, M.S. Johari, M. Zarrebini, Effect of 3D Fiber Orientation on Permeability of Realistic Fibrous Porous Networks, Powder Technol., 254 (2014) 44-56.

[22] H. Darcy, Les Fontaines Publiques de la Ville de Dijon, Delmont, Paris, 1856.

[23] R. Masoodi, K.M. Pillai, Wicking in Porous Materials: Traditional and Modern Modeling Approaches, CRC Press, Milwaukee2012.

[24] G.W. Jackson, D.F. James, The Permeability of Fibrous Porous Media, Can. J. Chem. Eng., 64 (1986) 364-374.

[25] S.L. Bryant, D.W. Mellor, C.A. Cade, Physical Representative Network Models of Transport in Porous Media, AlChE J., 39 (1993) 387-396.

[26] P. Soltani, M. Johari, M. Zarrebini, Tomography based Determination of Transverse Permeability in Fibrous Porous Media, J. Ind. Text., 44 (2013) 738-756

[27] B. Markicevic, T.D. Papathanasiou, The Hydraulic Permeability of Dual Porosity Fibrous Media, J. Reinf. Plast. Compos., 20 (2001) 871-880.

[28] A. Nabovati, E.W. Llewellin, A.C.M. Sousa, A General Model for the Permeability of Fibrous Porous Media based on Fluid Flow Simulations using the Lattice Boltzmann Method, Composites Part A, 40 (2009) 860-869.

[29] A.L. Chernyakov, Fluid Flow through Three-dimensional Fibrous Porous Media, J. Exp. Theor. Phys., 86 (1998) 1156-1166.

[30] Q. Wang, B. Maze, H.V. Tafreshi, B. Pourdeyhimi, A Case Study of Simulating Nanoparticle Filtration via Spun-bonded Filter Media, Chem. Eng. Sci., 61 (2006) 871 – 4883.

[31] J. Wang, X. Zhang, A.G. Bengough, J.W. Crawford, Domain-decomposition Method for Parallel Lattice Boltzmann Simulation of Incompressible Flow in Porous Media, Phys. Rev. E: Stat. Nonlinear Soft Matter Phys., 72 (2005) 13-18.

[32] S. Zobel, B. Maze, H. Vahedi Tafreshi, Q. Wang, B. Pourdeyhimi, Simulating Permeability of 3-D Calendered Fibrous Structures, Chem. Eng. Sci., 62 (2007) 6285-6296.

[33] A.K. Pradhan, D. Das, R. Chattopadhyay, S.N. Singh, Effect of 3D fiber Orientation Distribution on Transverse Air Permeability of Fibrous Porous Media, Powder Technol., 221 (2012) 101-104.

[34] M.A. Van Doormaal, J.G. Pharoah, Determination of Permeability in Fibrous Porous Media Using the Lattice Boltzmann Method with Application to PEM Fuel Cells, Int. J. Numer. Methods Fluids, 59 (2009) 75-89.

[35] M.C. Faessel, F.B. Delisee, P. Castera, 3D Modelling of Random Cellulosic Fibrous Networks based on X-ray Tomography and Image Analysis, Compos. Sci. Technol., 65 (2005) 1931–1940.

[36] F. Khan, F. Enzmann, M. Kersten, A. Wiegmann, K. Steiner, 3D Simulation of the Permeability Tensor in a Soil Aggregate on basis of Nanotomographic Imaging and LBE Solver, J. Soils Sediments, 12 (2012) 86-96.

[37] R. Moreno-Atanasio, R.A. Williams, X. Jia, Combining X-ray Microtomography with Computer Simulation for Analysis of Granular and Porous Materials, Particuology, 8 (2010) 81–99.

[38] P. Rama, Y. Liu, R. Chen, H. Ostadi, K. Jiang, X. Zhang, Y. Gao, P. Grassini, D. Brivio, Determination of the anisotropic permeability of a carbon cloth gas diffusion layer through X-ray computer micro-tomography and single-phase Lattice Boltzmann simulation, Int. J. Numer. Methods Fluids, 67 (2011) 518-530.

23

[39] http://www.mahoot-ir.com/web/fa/content/default.asp, Mahoot Co.

[40] E.N. Landis, D.T. Keane, X-ray Microtomography, Mater. Charact., 61 (2010) 1305-1316.

[41] F. Rezanezhad, W.L. Quinton, J.S. Price, T.R. Elliot, D. Elrick, K.R. Shook, Influence of Pore Size and Geometry on Peat Unsaturated Hydraulic Conductivity Computed from 3D Computed Tomography Image Analysis, Hydrol. Processes, 24 (2010) 2983-2994.

[42] C.L. Lin, J.D. Miller, Pore Structure and Network Analysis of Filter Cake, Chem. Eng. J., 80 (2000) 221-231.

[43] C. Selomulya, X. Jia, R.A. Williams, Direct Prediction of Structure and Permeability of Flocculated Structures and Sediments Using 3D Tomographic Imaging, Chem. Eng. Res. Des., 83 (2005) 844-852.

[44] R.M. Lewitt, Reconstruction Algorithms: Transform Methods, Proceedings of the IEEE, 71 (1983) 390-408.

[45] L. Salvo, P. Cloetens, E. Maire, S. Zabler, J.J. Blandin, J.Y. Buffière, W. Ludwig, E. Boller, D. Bellet, C. Josserond, X-ray Micro-tomography an Attractive Characterisation Technique in Materials Science, Nucl. Instrum. Methods Phys. Res., Sect. B, 200 (2003) 273-286.

[46] M.S. Islam, R. Caulkin, X. Jia, M. Fairweather, R.A. Williams, Prediction of the Permeability of Packed Beds of Non-Spherical Particles, Comput. Aided Chem. Eng., 30 (2012) 1088–1092.

[47] M. Mehrabi, M. Pasha, X. Jia, A. Hassanpour, Pore Volume Analysis of Gas Shale Samples using 3-D X-ray Micro Tomography, SPE Offshore Europe Conference and Exhibition, Society of Petroleum Engineers, 2015.

[48] R. Caulkin, X. Jia, M. Fairweather, R.A. Williams, Predictions of Porosity and Fluid Distribution through Nonspherical Packed Columns, AIChE J., 58 (2012) 1503-1512.

[49] W.K. Pratt, Digital Image Processing, Wiley-Inter Science Publication, New York2001.

[50] J.C. Tan, J.A. Elliott, T.W. Clyne, Analysis of Tomography Images of Bonded Fibre Networks to Measure Distributions of Fibre Segment Length and Fibre Orientation, Adv. Eng. Mater., 8 (2006) 495-500.

[51] J. Viguié, P. Latil, L. Orgéas, P.J.J. Dumont, S. Rolland du Roscoat, J.F. Bloch, C. Marulier, O. Guiraud, Finding Fibres and their Contacts within 3D Images of Disordered Fibrous Media, Compos. Sci. Technol., 89 (2013) 202-210.

[52] H. Yang, W.B. Lindquist, Three-dimensional Image Analysis of Fibrous Materials, Proc. SPIE: Applications of Digital Image Processing, San Diego. USA., 2000, pp. 275-282.

[53] T.C. Lee, R.L. Kashyap, C.N. Chu, Building Skeleton Models via 3-D Medial Surface Axis Thinning Algorithms, CVGIP-Graph. Model IM 56 (1994) 462-478.

[54] P. Soltani, M.S. Johari, M. Zarrebini, 3D Fiber Orientation Characterization of Nonwoven Fabrics using X-ray Micro-computed Tomography, World J. Text Eng. Technol., 1 (2015) 41-47.

[55] B. Pourdeyhimi, R. Ramanathan, R. Dent, Measuring Fiber Orientation in Nonwovens, Part II: Direct Tracking, Text. Res. J., 66 (1996) 747-753.

[56] B. Pourdeyhimi, R. Dent, H. Davis, Measuring Fiber Orientation in Nonwovens, Part III: Fourier Transform, Text. Res. J., 67 (1997) 143-151.

[57] B. Pourdeyhimi, R. Dent, Measuring Fiber Orientation in Nonwovens, Part IV: Flow Field Analysis, Text. Res. J., 67 (1997) 181-187.

[58] B. Pourdeyhimi, R. Dent, A. Jerbi, S. Tanaka, A. Deshpande, Measuring Fiber Orientation in Nonwovens, Part V: Real Webs, Text. Res. J., 69 (1999) 185-192.

[59] B. Pourdeyhimi, H.S. Kim, Measuring Fiber Orientation in Nonwovens: The Hough Transform, Text. Res. J., 72 (2002) 803-809.

[60] T. Komori, K. Marishima, Estimation of Fiber Orientation and Length in Fiber Assemblies, Text. Res. J., 48 (1978) 309-314.

[61] S.G. Advani, C.L. Tucker, The Use of Tensors to Describe and Predict Fiber Orientation in Short Fiber Composites, J. Rheol., 31 (1987) 751-784.

[62] M. Ziabari, V. Mottaghitalab, A.K. Haghi, Distance Transform Algorithm for Measuring Nanofiber Diameter, Korean J. Chem. Eng., 25 (2008) 905-918.

[63] Anonymous, Powder Technol., (2014).

[64] Anonymous, J. Ind. Text., (2015).

[65] S.D. Clague, R.J. Phillips, A Numerical Calculation of the Hydraulic Permeability of Three Dimensional Disordered Fibrous Media, Phys. Fluids, 9 (1997) 1562-1572.

[66] H. Vahedi Tafreshi, A.M.S. Rahman, S. Jaganathan, Q. Wang, B. Pourdeyhimi, Analytical Expressions for Predicting Permeability of Bimodal Fibrous Porous Media, Chem. Eng. Sci., 64 (2009) 1154-1159.

[67] C.N. Davies, The Separation of Airborne Dust and Particle, Proceedings of Institute of Mechanical Engineers, London, England, 1952, pp. 185-213.

[68] M.M. Tomadakis, J.T. Robertson, Viscous Permeability of Random Fiber Structures: Comparison of Electrical and Diffusional Estimates with Experimental and Analytical Results, J. Compos. Mater., 39 (2005) 163–188.

[69] L. Spielman, S.L. Goren, Model for Predicting Pressure Drop and Filtration Efficiency in Fibrous Media, Environ. Sci. Technol., 2 (1968) 279-287.

[70] A. Tamayol, M. Bahrami, Transverse Permeability of Fibrous Porous Media, Biophys. Rev., 83 (2011) 046314-046322.

[71] J.T. Gostick, M.W. Fowler, M.D. Pritzker, M.A. Ioannidis, L.M. Behra, In-plane and Through-plane Gas Permeability of Carbon Fiber Electrode Backing Layers, J. Power Sources, 162 (2006) 228-238.

[72] R.P. Labrecque, The Effects of Fiber Cross-Sectional Shape on the Resistance to the Flow of Fluids through Fiber Mats, Tappi J., 51 (1986) 8-18.

[73] A.G. Kostornov, M.S. Shevchuk, Hydraulic Characteristics and Structure of Porous Metal Fiber Materials, Part II: Effects of Porosity, Thickness, and Differential Pressure on the Principal Properties of Permeable Fiber Materials, Sov. Powder Metall. Met. Ceram., 12 (1973) 752-756.

[74] A.G. Kostornov, M.S. Shevchuk, Hydraulic Characteristics and Structure of Porous Metal Fiber Materials, Part III: Laws of Liquid Permeability of Materials, Sov. Powder Metall. Met. Ceram., 16 (1977) 694-699.

[75] W.B. Young, K. Rupel, K. Han, L.J. Lee, M.J. Liou, Analysis of Resin Injection Molding in Molds with Preplaced Fiber Mats, Part II: Numerical Simulation and Experiments of Mold Filling, Polym. Compos., 12 (1991) 30-38.

[76] A. Tamayol, M. Bahrami, In-plane Gas Permeability of Proton Exchange Membrane Fuel Cell Gas Diffusion Layers, J. Power Sources, 196 (2011) 3559-3564.

[77] R. Gauvin, F. Trochu, Y. Lemenn, L. Diallo, Permeability Measurement and Flow Simulation through Fiber Reinforcement, Polym. Compos., 17 (1996) 34-42.

[78] C.H. Shih, L.J. Lee, Effect of Fiber Architecture on Permeability in LCM, Polym. Compos., 19 (1998) 626-639.

[79] J.P. Feser, A.K. Prasad, S.G. Advani, Experimental Characterization of In-plane Permeability of Gas Diffusion Layers, J. Power Sources, 162 (2006) 1226-1231.
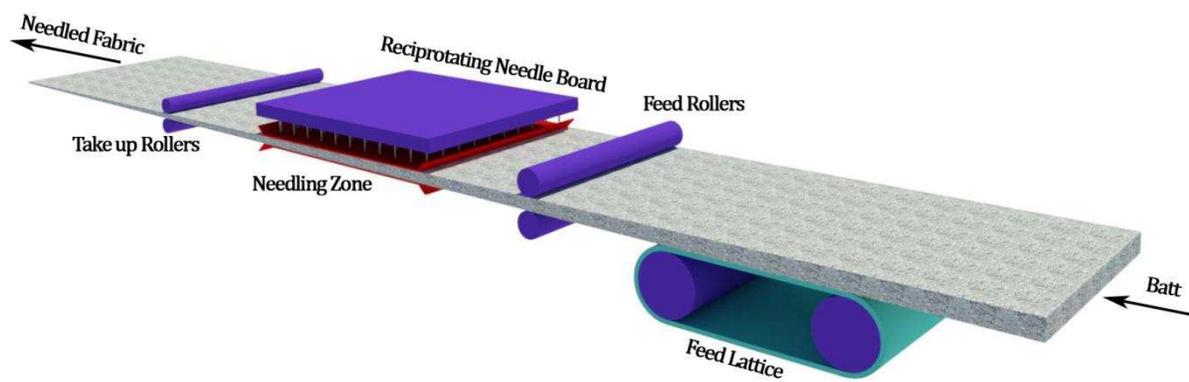
Figure 1: Schematic of needle punching process
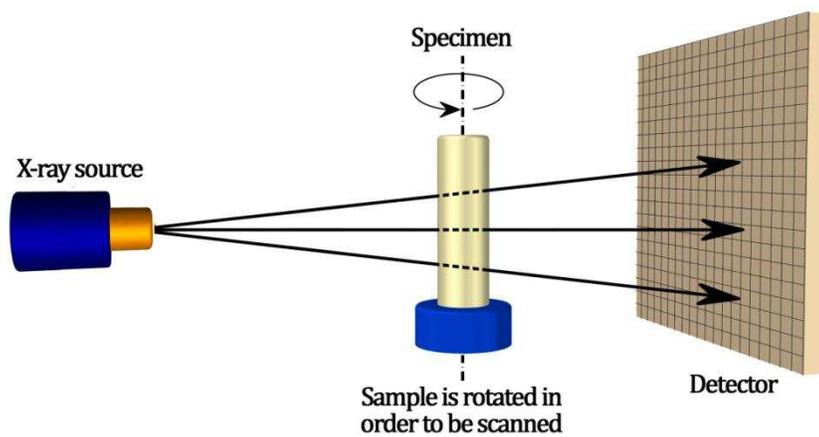
Figure 2: Schematic diagram of μCT
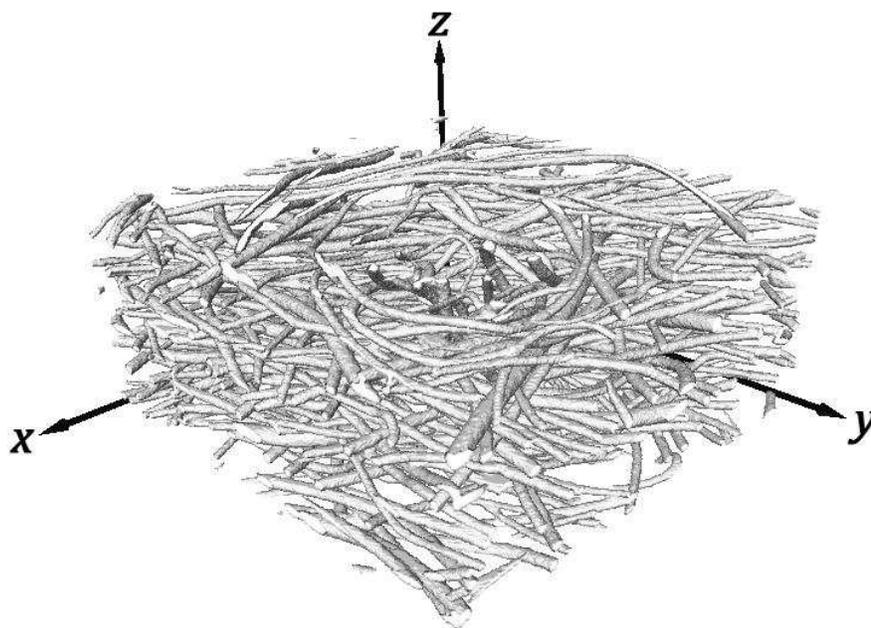
Figure 3: 3D tomographic reconstruction of nonwoven fabric (realistic structure)
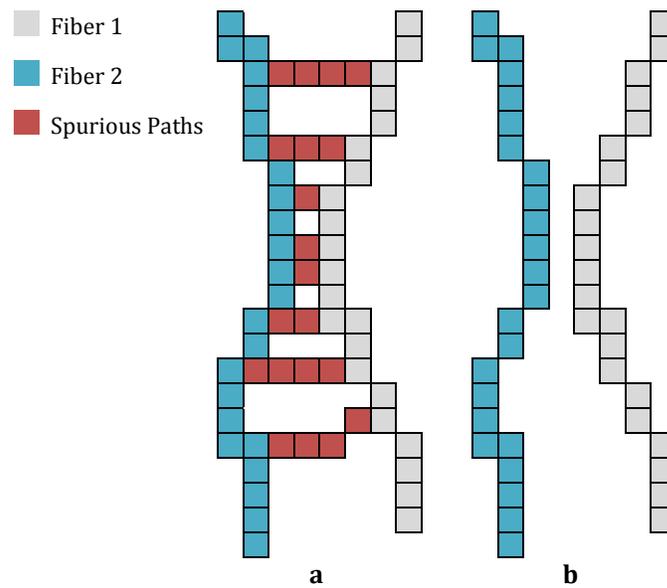
Figure 4: a) ladder-shaped medial axis formed by two fibers touching at an acute angle of incidence; b) removing spurious paths after applying surface remnant reduction algorithm
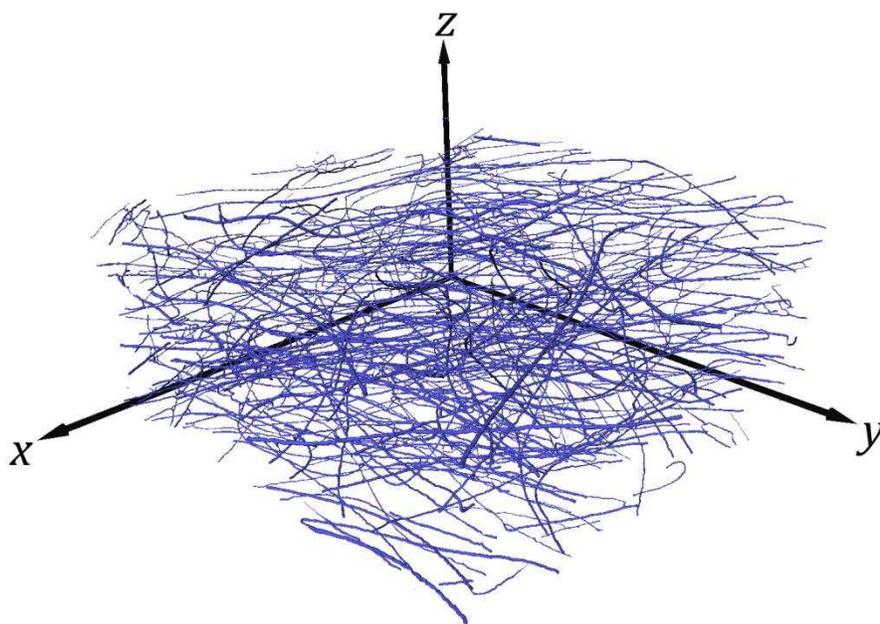
Figure 5: Skeletonized structure of nonwoven fabric shown in Fig. 3
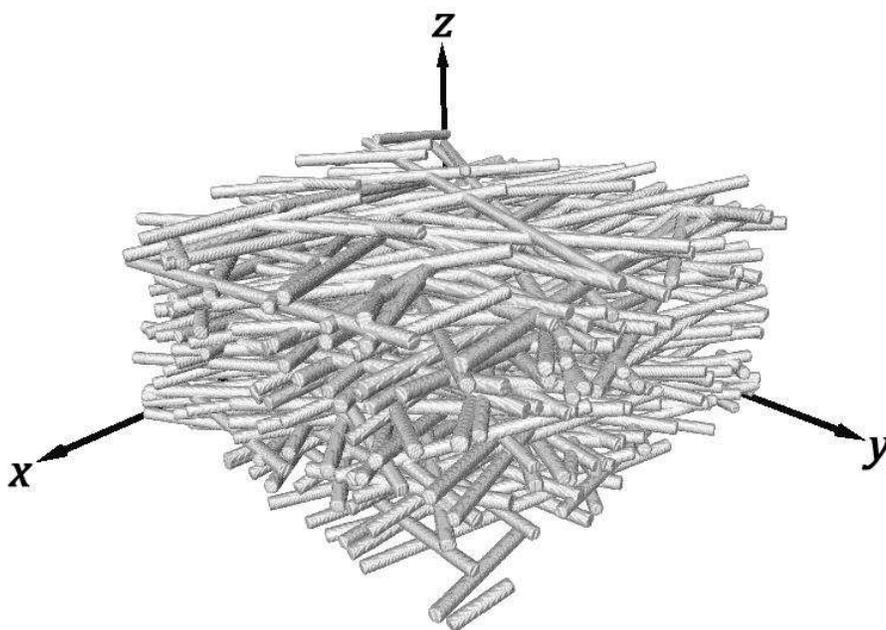
Figure 6: Nonwoven virtual 3D structure
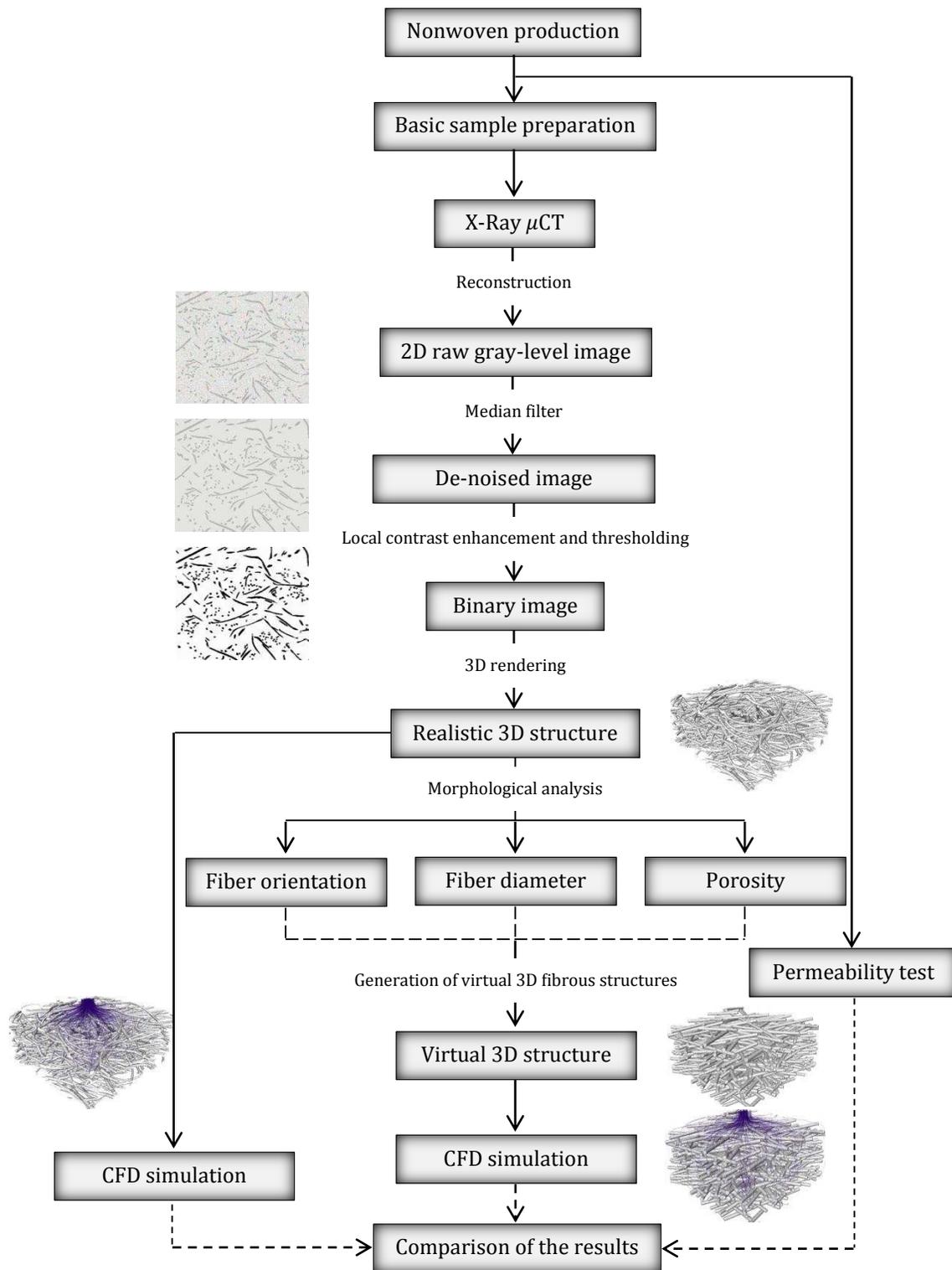
Figure 7: X-ray μCT, image processing, virtual structure generation and CFD simulation flowchart
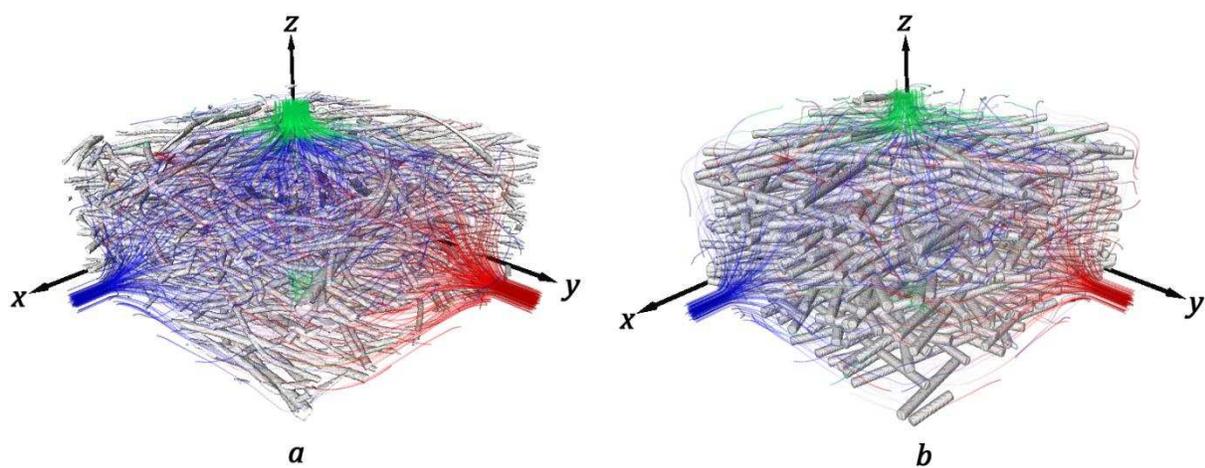
Figure 8: Fluid flow streamlines through a) realistic and b) virtual structure
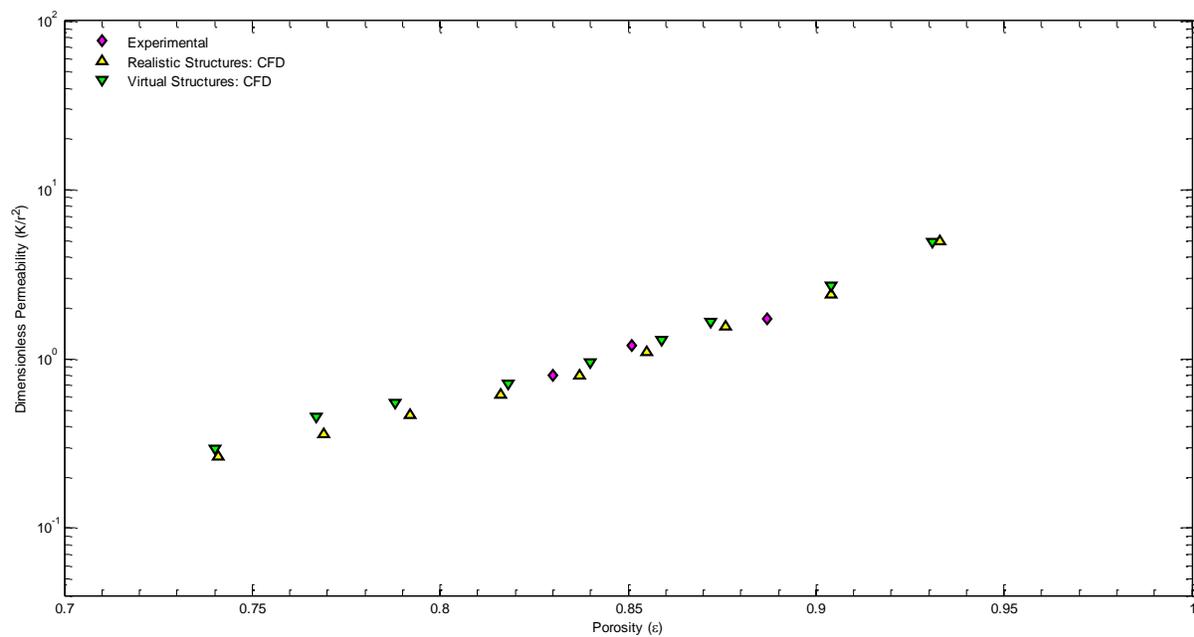
Figure 9: Through-plane dimensionless permeability as a function of porosity of layered structures
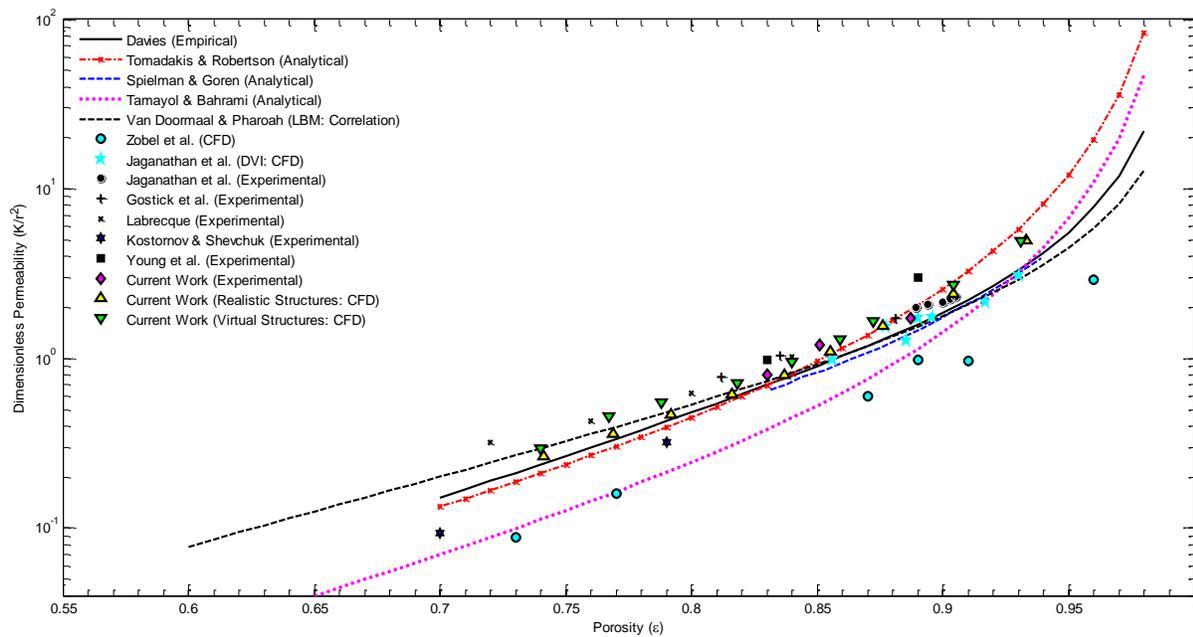
Figure 10: Comparison of through-plane dimensionless permeabilities of realistic and virtual layered structures with those of available published empirical, analytical, numerical and experimental studies
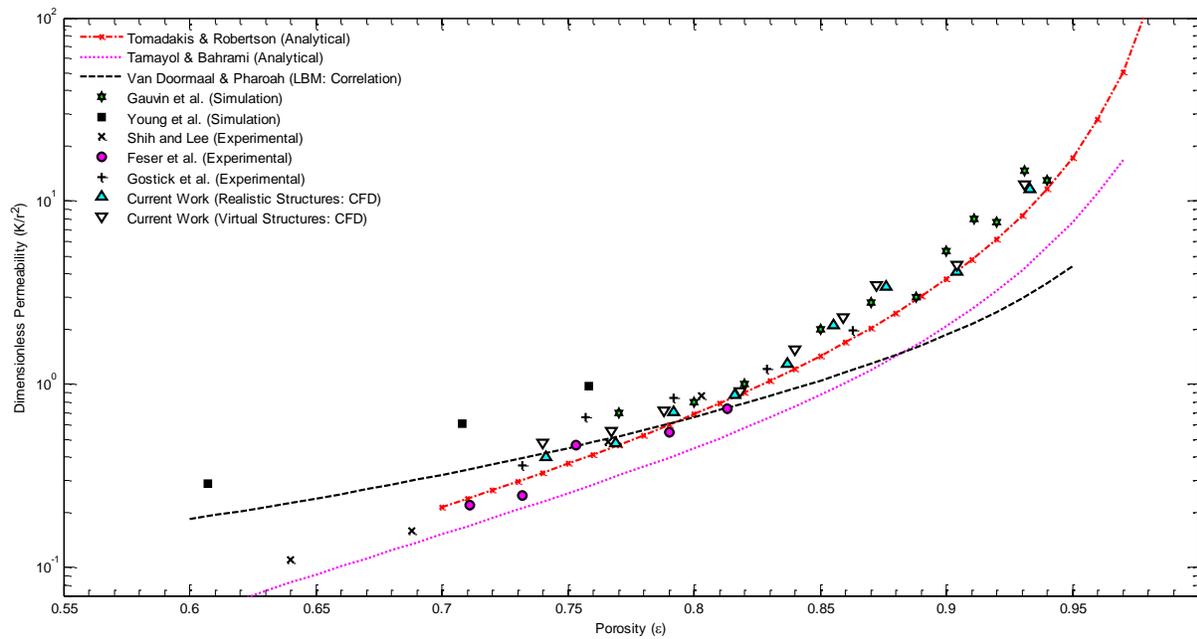
Figure 11: Comparison of in-plane dimensionless permeabilities of realistic and virtual layered structures with those of available published analytical, numerical and experimental studies
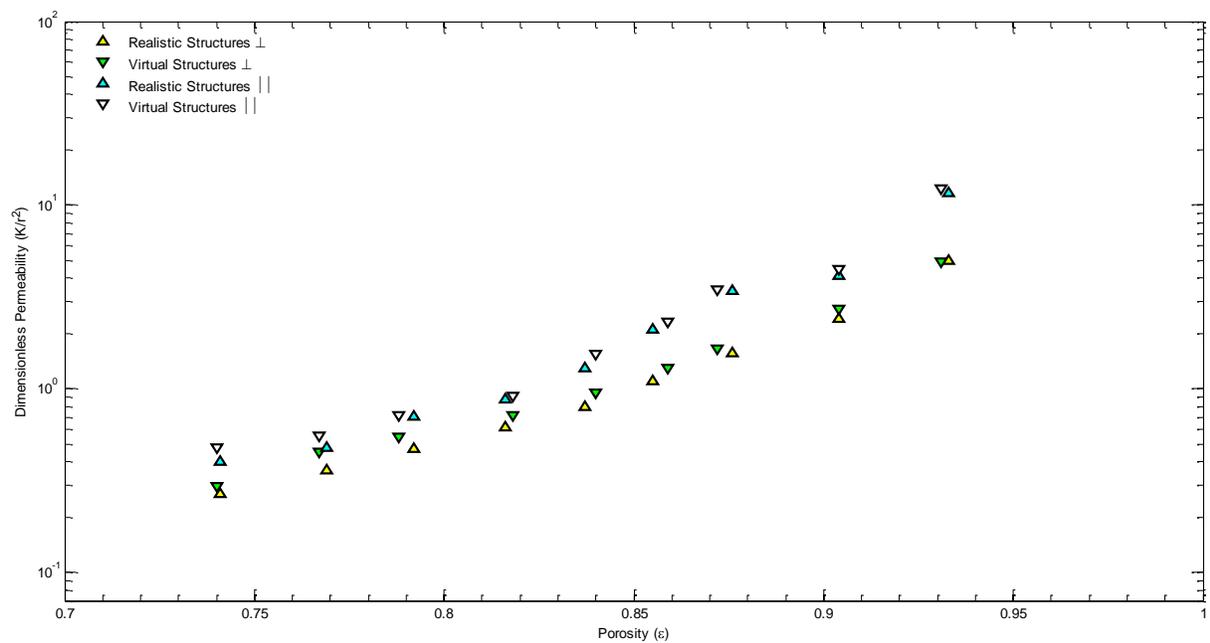
Figure 12: Comparison of through- and in-plane permeability of realistic and virtual structures

Table 1 *μ*CT scanning settings

Parameter	Unit	*μ*CT
Sample size	mm^3	5×5×fabric thickness
Voxel size (resolution)	*μ*m	3
Angular step	degree	1
Voltage	kV	90
Exposure time	ms	500
Scan time	minute	210

Table 2 Structural characteristics of realistic and virtual structures

Sample	Porosity	Ω_{xx}	Ω_{yy}	Ω_{zz}	Sample	Porosity	Ω_{xx}	Ω_{yy}	Ω_{zz}
R_1	0.741	0.45	0.49	0.06	V_1	0.740	0.45	0.48	0.07
R_2	0.769	0.44	0.49	0.07	V_2	0.767	0.44	0.48	0.08
R_3	0.792	0.44	0.47	0.09	V_3	0.787	0.44	0.45	0.11
R_4	0.816	0.43	0.48	0.09	V_4	0.818	0.43	0.46	0.11
R_5	0.837	0.43	0.47	0.10	V_5	0.840	0.44	0.46	0.10
R_6	0.855	0.44	0.45	0.11	V_6	0.859	0.45	0.43	0.12
R_7	0.876	0.43	0.45	0.12	V_7	0.872	0.42	0.45	0.13
R_8	0.904	0.44	0.41	0.15	V_8	0.904	0.43	0.41	0.16
R_9	0.933	0.41	0.42	0.17	V_9	0.931	0.41	0.41	0.18

* R and V denote realistic and virtual structures, respectively